

# Polarized line formation in multi-dimensional media-II: *A fast method to solve problems with partial frequency redistribution*

L. S. Anusha<sup>1</sup> and K. N. Nagendra<sup>1</sup>

<sup>1</sup>*Indian Institute of Astrophysics, Koramangala, 2nd Block, Bangalore 560 034, India*  
and

F. Paletou<sup>2</sup>

<sup>2</sup>*Laboratoire d'Astrophysique de Toulouse-Tarbes, Université de Toulouse, CNRS, 14 av. E. Belin, 31400 Toulouse, France.*

## ABSTRACT

In the previous paper of this series (Anusha & Nagendra 2010), we presented a formulation of the polarized radiative transfer equation for resonance scattering with partial frequency redistribution (PRD) in multi-dimensional media for a two-level atom model with unpolarized ground level, using the irreducible spherical tensors  $\mathcal{T}_Q^K(i, \mathbf{\Omega})$  for polarimetry. We also presented a polarized approximate lambda iteration (PALI) method to solve this equation using the Jacobi iteration scheme. The formal solution used was based on a simple finite volume technique.

In this paper, we develop a faster and more efficient method which uses the projection techniques applied to the radiative transfer equation (the Stabilized Preconditioned Bi-Conjugate Gradient method). We now use a more accurate formal solver, namely the well known 2D (two dimensional) short characteristics method.

Using the numerical method developed in Anusha & Nagendra (2010), we can consider only simpler cases of finite 2D slabs due to computational limitations. Using the method developed in this paper we could compute PRD solutions in 2D media, in the more difficult context of semi-infinite 2D slabs as well. We present several solutions which may serve as benchmarks in future studies in this area.

*Subject headings:* line: formation – radiative transfer – polarization – scattering– Sun: atmosphere

## 1. Introduction

The observations of the solar atmosphere indicate the existence of small scale structures, which break the spatial homogeneity of the atmosphere. Since these structures have different physical properties, one can expect the effect of lateral transport of radiation to be rather important. Extensive studies on radiative transfer in 2D (two dimensional) and 3D (three dimensional) geometries have been made to understand the intensity profiles in spectroscopic observations. As the polarization of the radiation field is more sensitive to the breaking of axisymmetry occurring in 2D and 3D geometries than the intensity (Stokes

$I$  parameter), the solution of polarized radiative transfer equation in 2D and 3D geometries is very much needed for the understanding of the spectropolarimetric observations. Polarized radiative transfer problems have been addressed in the past decade, but only for complete frequency redistribution (CRD). A first investigation with partial frequency redistribution (PRD), for 3D geometry, is described in (Anusha & Nagendra 2010, hereafter called Paper 1). Solving polarized transfer equation with PRD in multi-dimensional geometries is numerically expensive, both in terms of computing time and the computer memory. To address this problem, in this paper we develop a

numerical method for 2D geometry which is faster than the Jacobi iteration method used in Paper 1. The method developed here can be easily extended to 3D geometries. For reviews on iterative methods see Trujillo Bueno (2003); Nagendra & Sampurna (2009) and references cited therein. For a detailed historical account of the developments in the area of multidimensional radiative transfer we refer to Paper 1.

For 2D geometry, Paletou et al. (1999) solve the polarized line transfer equation for the Stokes  $I, Q, U$  parameters, with CRD, using a perturbation technique combined with a short characteristics formal solution method. We generalize their work in following respects. We include PRD, and solve the radiative transfer problem using a decomposition of the Stokes parameters into a set of irreducible components. This Stokes vector decomposition for multi-dimensional geometries was developed in Paper 1. Its main advantage is that the mean intensity components (averaged over all frequencies and directions of the incident radiation) become independent of the outgoing direction ( $\boldsymbol{\Omega}$ ) and also the scattering phase matrix. These properties have allowed us to set up an iterative method which is faster and more accurate than the previous methods.

First, instead of the perturbation method used in Paletou et al. (1999), and the Jacobi method used in Paper 1, we have implemented a new iterative method called the Stabilized Preconditioned Bi-Conjugate Gradient (Pre-BiCG-STAB) algorithm. The Pre-BiCG and Pre-BiCG-STAB methods belong to a class of iterative methods known as projection techniques. Projection methods have already proved their usefulness for unpolarized transfer problems with the CRD approximation in different geometries (see e.g. Klein et al. 1989; Folini 1998; Papkalla 1995; Meinkhon 2009; Hubeny & Burrows 2007; Paletou & Anterrieu 2009; Anusha et al. 2009). Polarization was considered in Nagendra et al. (2009) for planar geometry. Second, we have generalized the 2D short characteristics formal solver of Paletou et al. (1999) to PRD. This 2D formal solver is more accurate than the formal solver used in Paper 1.

The organization of the paper is as follows. In Section 2 we present the governing equations. In Section 3 we describe the 2D short characteristics formal solution method. In Section 4 we give some

details of the computations. In Section 5 we discuss the Pre-BiCG-STAB algorithm. Section 6 is devoted to results and discussions.

## 2. The Polarized transfer equation in a 2D medium

We consider radiative transfer in a 2D slab in Cartesian geometry. We assume that the medium is infinite in  $X$  direction and finite in  $Y$  and  $Z$  directions (see Figure 1). This means that any two  $YZ$  planes at two different points on the  $X$  axis are identical. As a result, all the physical quantities like the Stokes vector  $\mathbf{I}$ , the source vector  $\mathbf{S}$  remain independent of the  $X$  co-ordinate. We assume that our 2D slab is situated at  $x = x_0$ . For a given ray with direction  $\boldsymbol{\Omega}$ , the transfer equation in divergence form in the atmospheric reference frame may be written as

$$\begin{aligned} \boldsymbol{\Omega} \cdot \nabla \mathbf{I}(\mathbf{r}, \boldsymbol{\Omega}, x) = \\ -[\kappa_l(\mathbf{r})\phi(x) + \kappa_c(\mathbf{r})][\mathbf{I}(\mathbf{r}, \boldsymbol{\Omega}, x) - \mathbf{S}(\mathbf{r}, \boldsymbol{\Omega}, x)], \end{aligned} \quad (1)$$

where  $\mathbf{I} = (I, Q, U)^T$  is the Stokes vector. We choose positive Stokes  $Q$  to be in the direction perpendicular to the surface defined by  $z = Z_{max}$ . Here  $\mathbf{r} = (x, y, z)$  is the position vector of the ray.  $\boldsymbol{\Omega} = (\eta, \gamma, \mu) = (\sin \theta \cos \varphi, \sin \theta \sin \varphi, \cos \theta)$  describes the direction cosines of the ray with respect to the atmospheric normal  $Z$ , with  $\theta, \varphi$  being the polar and azimuthal angles of the ray (see Figure 3(b)). The Stokes  $V$  parameter decouples from the other three. We confine our attention in this paper to the polarized transfer equation for  $(I, Q, U)^T$ . We represent the frequency averaged line opacity and continuum opacity by  $\kappa_l$  and  $\kappa_c$  respectively, and the profile function by  $\phi$ . Frequency is measured in Doppler width units from the line center and is denoted by  $x$ , with the Doppler width being constant in the atmosphere. It is convenient to work with the transfer equation written along a ray path. It has the form

$$\frac{d\mathbf{I}(\mathbf{r}, \boldsymbol{\Omega}, x)}{ds} = -\kappa_{tot}(\mathbf{r}, x)[\mathbf{I}(\mathbf{r}, \boldsymbol{\Omega}, x) - \mathbf{S}(\mathbf{r}, \boldsymbol{\Omega}, x)], \quad (2)$$

where  $s = \sqrt{x^2 + y^2 + z^2}$  is the path length along the ray. The total opacity  $\kappa_{tot}(\mathbf{r}, x)$  is given by

$$\kappa_{tot}(\mathbf{r}, x) = \kappa_l(\mathbf{r})\phi(x) + \kappa_c(\mathbf{r}). \quad (3)$$

The formal solution of Equation (2) is given by

$$\begin{aligned} \mathbf{I}(\mathbf{r}, \boldsymbol{\Omega}, x) &= \mathbf{I}(\mathbf{r}_0, \boldsymbol{\Omega}, x) e^{-\int_{s_0}^s \kappa_{tot}(\mathbf{r} - s''\boldsymbol{\Omega}, x) ds''} \\ &+ \int_{s_0}^s \mathbf{S}(\mathbf{r} - s'\boldsymbol{\Omega}, \boldsymbol{\Omega}, x) e^{-\int_{s'}^s \kappa_{tot}(\mathbf{r} - s''\boldsymbol{\Omega}, x) ds''} \\ &\times [\kappa_{tot}(\mathbf{r} - s'\boldsymbol{\Omega}, x)] ds'. \end{aligned} \quad (4)$$

$\mathbf{I}(\mathbf{r}_0, \boldsymbol{\Omega}, x)$  is the boundary condition imposed at  $\mathbf{r}_0 = (x_0, y_0, z_0)$  (see Figure 2).

In a two-level atom model with unpolarized ground level, the total source vector  $\mathbf{S}$  is given by

$$\mathbf{S}(\mathbf{r}, \boldsymbol{\Omega}, x) = \frac{\kappa_l(\mathbf{r})\phi(x)\mathbf{S}_l(\mathbf{r}, \boldsymbol{\Omega}, x) + \kappa_c(\mathbf{r})\mathbf{S}_c(\mathbf{r}, x)}{\kappa_l(\mathbf{r})\phi(x) + \kappa_c(\mathbf{r})}. \quad (5)$$

Here  $\mathbf{S}_c$  is the continuum source vector given by  $(B(\mathbf{r}), 0, 0)^T$  with  $B(\mathbf{r})$  the Planck function at the line center frequency. The line source vector can be expressed as

$$\begin{aligned} \mathbf{S}_l(\mathbf{r}, \boldsymbol{\Omega}, x) &= \mathbf{G}(\mathbf{r}) + \int_{-\infty}^{+\infty} dx' \\ &\times \oint \frac{d\boldsymbol{\Omega}'}{4\pi} \frac{\hat{R}(x, x', \boldsymbol{\Omega}, \boldsymbol{\Omega}')}{\phi(x)} \mathbf{I}(\mathbf{r}, \boldsymbol{\Omega}', x'), \end{aligned} \quad (6)$$

where  $\mathbf{G} = (\epsilon B(\mathbf{r}), 0, 0)^T$  is the thermal source.  $\epsilon = \Gamma_I / (\Gamma_R + \Gamma_I)$  with  $\Gamma_I$  and  $\Gamma_R$  the inelastic collisional de-excitation rate and the radiative de-excitation rate respectively, so that  $\epsilon$  represents the rate of photon destruction by inelastic collisions, also known as the thermalization parameter. We assume that  $\phi$  is a Voigt function. It depends on the damping parameter  $a$ , given by  $a = a_R [1 + (\Gamma_E + \Gamma_I) / \Gamma_R]$  where  $a_R = \Gamma_R / 4\pi\Delta\nu_D$  and  $\Gamma_E$  is the elastic collision rate. As the lower level is assumed to be infinitely sharp, the radiative, and collisional rates refer only to the upper level.  $\hat{R}$  is the redistribution matrix given in Domke & Hubeny (1988); Bommier (1997). The solid angle element  $d\boldsymbol{\Omega}' = \sin\theta' d\theta' d\varphi'$ ,  $\theta \in [0, \pi]$  and  $\varphi \in [0, 2\pi]$  (see Figure 3(b)). After decomposition of the vectors  $\mathbf{I}$  and  $\mathbf{S}$  into irreducible components following the method described in Paper 1, the redistribution matrix  $\hat{R}(x, x', \boldsymbol{\Omega}, \boldsymbol{\Omega}')$  can be factorized into the product of a matrix  $\hat{R}(x, x')$  and a phase matrix  $\hat{\Psi}(\boldsymbol{\Omega})$ . Its elements are given

by

$$\Psi_{QQ'}^{KK'}(\boldsymbol{\Omega}) = \sum_{j=0}^3 (\mathcal{T}_Q^K)^*(j, \boldsymbol{\Omega}) \mathcal{T}_{Q'}^{K'}(j, \boldsymbol{\Omega}). \quad (7)$$

Here  $\mathcal{T}_{Q'}^{K'}(j, \boldsymbol{\Omega})$  are irreducible spherical tensors for polarimetry with  $K = 0, 1, 2, -K \leq Q \leq +K$  (see Landi Degl'Innocenti & Landolfi 2004). In this paper, we consider only the linear polarization. Therefore,  $K = 0, 2$  and  $Q \in [-K, +K]$ . The matrix  $\hat{\Psi}(\boldsymbol{\Omega})$  is a  $6 \times 6$  matrix. Its elements and the irreducible components of  $\mathbf{I}$  and  $\mathbf{S}$  are complex quantities. We apply the transformation described in Frisch (2007) to transform these components and the elements of  $\hat{\Psi}(\boldsymbol{\Omega})$  matrix into real quantities. Hereafter we work with only real quantities. We keep the notation  $\hat{\Psi}(\boldsymbol{\Omega})$  for the phase matrix. We introduce the irreducible Stokes vector  $\mathcal{I} = (I_0^0, I_0^2, I_1^{2,x}, I_1^{2,y}, I_2^{2,x}, I_2^{2,y})^T$  and irreducible source vector  $\mathcal{S} = (S_0^0, S_0^2, S_1^{2,x}, S_1^{2,y}, S_2^{2,x}, S_2^{2,y})^T$ . The components of  $\mathcal{I}$  and  $\mathcal{S}$  are all real. The radiative transfer equation for the vector  $\mathcal{I}$  is given by

$$\begin{aligned} -\frac{1}{\kappa_{tot}(\mathbf{r}, x)} \boldsymbol{\Omega} \cdot \nabla \mathcal{I}(\mathbf{r}, \boldsymbol{\Omega}, x) &= \\ [\mathcal{I}(\mathbf{r}, \boldsymbol{\Omega}, x) - \mathcal{S}(\mathbf{r}, x)]. \end{aligned} \quad (8)$$

Here  $\mathcal{S}(\mathbf{r}, x) = p_x \mathcal{S}_l(\mathbf{r}, x) + (1 - p_x) \mathcal{S}_c(\mathbf{r}, x)$  with

$$\mathcal{S}_l(\mathbf{r}, x) = \epsilon \mathcal{B}(\mathbf{r}) + \mathcal{J}(\mathbf{r}, x), \quad (9)$$

where the mean intensity vector is

$$\begin{aligned} \mathcal{J}(\mathbf{r}, x) &= \frac{1}{\phi(x)} \int_{-\infty}^{+\infty} dx' \\ &\times \oint \frac{d\boldsymbol{\Omega}}{4\pi} \hat{R}(x, x') \hat{\Psi}(\boldsymbol{\Omega}) \mathcal{I}(\mathbf{r}, \boldsymbol{\Omega}, x'). \end{aligned} \quad (10)$$

$\mathcal{S}_c(\mathbf{r}, x) = (B(\mathbf{r}), 0, 0, 0, 0, 0)^T$  is the continuum source vector and  $\mathcal{B} = (B(\mathbf{r}), 0, 0, 0, 0, 0)^T$  is the Planck vector. We assume that the ratio  $\kappa_c(\mathbf{r}) / \kappa_l(\mathbf{r})$  is independent of  $\mathbf{r}$ . The parameter  $p_x$  is defined by

$$p_x = \kappa_l(\mathbf{r})\phi(x) / \kappa_{tot}(\mathbf{r}, x). \quad (11)$$

The 2D Cartesian geometry used here implies some symmetries which simplify the problem. The radiation field has a symmetry with respect to the

$X$  axis which leads to

$$\begin{aligned} I(\mathbf{r}, \theta, \varphi, x) &= I(\mathbf{r}, \theta, \pi - \varphi, x), \\ I(\mathbf{r}, \theta, \pi + \varphi, x) &= I(\mathbf{r}, \theta, 2\pi - \varphi, x), \\ \theta &\in [0, \pi], \varphi \in [0, \pi/2]. \end{aligned} \quad (12)$$

Because the thermal source vector is unpolarized, the above symmetry relation leads to the symmetry of Stokes  $Q$  and anti-symmetry of Stokes  $U$  (see Appendix B) namely

$$\begin{aligned} Q(\mathbf{r}, \theta, \varphi, x) &= Q(\mathbf{r}, \theta, \pi - \varphi, x), \\ Q(\mathbf{r}, \theta, \pi + \varphi, x) &= Q(\mathbf{r}, \theta, 2\pi - \varphi, x), \\ U(\mathbf{r}, \theta, \varphi, x) &= -U(\mathbf{r}, \theta, \pi - \varphi, x), \\ U(\mathbf{r}, \theta, \pi + \varphi, x) &= -U(\mathbf{r}, \theta, 2\pi - \varphi, x), \\ \theta &\in [0, \pi], \varphi \in [0, \pi/2]. \end{aligned} \quad (13)$$

Using Equations (12) and (13) we can prove that

$$J_1^{2,x} = 0, \quad J_2^{2,y} = 0. \quad (14)$$

Thus we have  $S_1^{2,x} = 0$  and  $S_2^{2,y} = 0$  and  $I_1^{2,x} = 0$  and  $I_2^{2,y} = 0$ . Thus in a 2D geometry, one needs to only 4 out of the 6 irreducible components to describe the linearly polarized radiation field. We recall that in a 3D geometry all the 6 irreducible components are non-zero (see Paper 1).

The matrix  $\hat{R}$  is diagonal. It is given by

$$\hat{R}(x, x') = \hat{W}[\hat{\alpha}r_{\text{II}}(x, x') + (\hat{\beta} - \hat{\alpha})r_{\text{III}}(x, x')], \quad (15)$$

where

$$\hat{W} = \text{diag}\{W_0, W_2, W_2, W_2\}, \quad (16)$$

$$\hat{\alpha} = \text{diag}\{\alpha, \alpha, \alpha, \alpha\}, \quad (17)$$

$$\hat{\beta} = \text{diag}\{\beta^{(0)}, \beta^{(2)}, \beta^{(2)}, \beta^{(2)}\}. \quad (18)$$

The weight  $W_0 = 1$  and the weights  $W_2$  depend on the line under consideration (see Landi Degl'Innocenti & Landolfi 2004). Here  $r_{\text{II}}(x, x')$  and  $r_{\text{III}}(x, x')$  are the angle-averaged redistribution functions introduced by Hummer (1962). The branching ratios are given by

$$\alpha = \frac{\Gamma_R}{\Gamma_R + \Gamma_E + \Gamma_I}, \quad (19)$$

$$\beta^{(K)} = \frac{\Gamma_R}{\Gamma_R + D^{(K)} + \Gamma_I}, \quad (20)$$

with  $D^{(0)} = 0$  and  $D^{(2)} = c\Gamma_E$ , where  $c$  is a constant, taken to be 0.379 (see Faurobert-Scholl 1992).

### 3. A short characteristics method for 2D radiative transfer

In this section we discuss the short characteristics formal solver used here. The first 2D short characteristics formal solver was introduced by Mihalas et al. (1978) for scalar radiative transfer and an improved version was given in Kunasz & Auer (1988). A further improvement with the introduction of monotonic interpolation was proposed by Auer & Paletou (1994). Then Auer et al. (1994) generalized it to the case of 3D geometry. The extension to include polarization in 2D geometries was done by Paletou et al. (1999) for Rayleigh scattering and by Manso Sainz & Trujillo Bueno (1999) and Dittmann (1999) for the Hanle effect in 2D and 3D geometries. All the above papers use CRD as the scattering mechanism. PRD was introduced for the scalar case by Auer & Paletou (1994). In this paper we generalize to the PRD scattering, the method of Paletou et al. (1999).

A short characteristics stencil MOP of a ray passing through the point O, projected on to the 2D plane is shown in Figure 3(a). The point O is always chosen to coincide with a grid point along the ray path. The points M and P intersect the boundaries of the 2D cells either on a horizontal line or on a vertical line, depending on the direction cosines of the given ray. The length  $\Delta s$  of the line segment MO or OP is simply,

$$\Delta s = \Delta z / \mu, \quad \text{if the ray hits the horizontal line,} \quad (21)$$

and

$$\Delta s = \Delta y / \gamma, \quad \text{if the ray hits the vertical line.} \quad (22)$$

Here  $\Delta z$  and  $\Delta y$  are increments (positive or negative) between two successive grid points in  $Z$  and  $Y$  directions respectively. Figure 3(b) shows the angles  $\theta$  and  $\varphi$  that define the orientation of a ray that passes through the point O. Figure 3(b) also shows all the 8 octants contributing to the radiation field at O. The cone of rays above the point O corresponds to  $\mu < 0$ , and the one below the point O corresponds to  $\mu > 0$ . Each of these cones is further divided into 4 regions, which are defined by  $\varphi \in [0, \pi/2]$ ,  $[\pi/2, \pi]$ ,  $[\pi, 3\pi/2]$ ,  $[3\pi/2, 2\pi]$ . In the short characteristics method, the irreducible

Stokes vector  $\mathcal{I}$  at O is given by

$$\begin{aligned} \mathcal{I}(\mathbf{r}, \boldsymbol{\Omega}, x) &= \mathcal{I}_M(\mathbf{r}, \boldsymbol{\Omega}, x) \exp[-\Delta\tau_M] \\ &+ \psi_M(\mathbf{r}, \boldsymbol{\Omega}, x) \mathcal{S}_M(\mathbf{r}, \boldsymbol{\Omega}, x) \\ &+ \psi_O(\mathbf{r}, \boldsymbol{\Omega}, x) \mathcal{S}_O(\mathbf{r}, \boldsymbol{\Omega}, x) \\ &+ \psi_P(\mathbf{r}, \boldsymbol{\Omega}, x) \mathcal{S}_P(\mathbf{r}, \boldsymbol{\Omega}, x), \end{aligned} \quad (23)$$

where  $\mathcal{S}_{M,O,P}$  are the irreducible source vectors at M, O and P. The quantity  $\mathcal{I}_M$  is the upwind irreducible Stokes vector at the point O. If M and P are non-grid points, then,  $\mathcal{S}_{M,P}$  and  $\mathcal{I}_M$  are computed using a parabolic interpolation formula. While computing them, one has to ensure the monotonicity of all the 4 components of these vectors, by appropriate logical tests (see Auer & Paletou 1994). The coefficients  $\psi$  depend on the optical depth increments in  $Y$  and  $Z$  directions and are given in Auer & Paletou (1994).

#### 4. Computational details

To calculate the integral in Equation (9) and the formal solution in Equation (23), we need to define quadratures for angles, frequencies and depths.

##### 4.1. The angle quadrature in 2D/3D geometries

Performing angle integrations in 2D or 3D geometries is not a trivial task. We have to consider the distribution of the rays in the 3 dimensional angular space namely,  $\boldsymbol{\Omega} = (\eta, \gamma, \mu)$ . This is important because a correct representation of the incident radiation field from all the octants surrounding the point of interest O is essential. The same argument is valid also for the radiation emerging from the point O. A Gaussian quadrature, because it tends to distribute more points near the limits of integration, is not appropriate to correctly represent the radiation field in all the 8 octants. The special quadrature method developed by Carlsson (1963) for neutron transport is much superior in this respect. For all the computations presented in this paper, Carlsson type B quadrature with the order  $n = 8$  is used. In the first octant, the  $\theta$  and  $\varphi$  grid points are computed using

$$\theta = \arccos |\mu|, \quad (24)$$

and

$$\varphi = \arctan |\gamma/\eta|. \quad (25)$$

The values of the quadrature points  $(\eta_i, \gamma_i, \mu_i)$  in the first octant ( $\theta \in [0, \pi/2]$ ,  $\varphi \in [0, \pi/2]$ ) and the respective weights  $w_i$  are given in Table 1. The values of corresponding  $\theta_i$  and  $\varphi_i$  are also listed.

The angle points in the other octants can be easily computed using simple trigonometric formulas. We have found that the order  $n = 8$  provides a good accuracy for the solution. These quadrature points can be used in 2D as well as 3D transfer computations.

##### 4.2. The spatial and frequency gridding

In this paper, we use a logarithmic spacing in  $Y$  and  $Z$  directions, with a fine gridding near the boundaries. The  $X$  direction is taken to be infinitely extended. We recall that the polarized radiation field depends on  $Y$  and  $Z$  co-ordinates, but is independent of the  $X$  co-ordinate.

For most of the results presented in this paper, a damping parameter of the Voigt profile function,  $a = 10^{-3}$  is used. The number of frequency points required for a problem depends on the value of  $a$  and the optical thickness in  $Y$  and  $Z$  directions (denoted by  $T_Y$  and  $T_Z$ ). A frequency bandwidth satisfying the conditions  $\phi(x_{max})T_Y \ll 1$  and  $\phi(x_{max})T_Z \ll 1$  at the largest frequency point denoted by  $x_{max}$  has been used. We have used a logarithmic frequency grid with a fine spacing in the line core region and the near wings where the PRD effects are important.

#### 5. A Preconditioned BiCG-STAB method

The Pre-BiCG (Preconditioned Bi-Conjugate Gradient) and Pre-BiCG-STAB (Preconditioned Bi-Conjugate Gradient-Stabilized) are iterative methods based on projections of residual vectors on Krylov subspaces (see Saad 2000). We recall that a great advantage of the Pre-BiCG-STAB method is that, unlike the Pre-BiCG method, it does not require the construction and storage of the transpose of  $\hat{A}$  matrix, where  $\hat{A}$  is the matrix of the system of equations to be solved (see below). The Pre-BiCG and Pre-BiCG-STAB methods have been applied up to now to radiative transfer problems with CRD (see Introduction for references). In this paper we generalize the computing algorithm of the Pre-BiCG-STAB method

to polarized radiative transfer with PRD in a 2D medium and show that this method is quite efficient.

Using the formal solution expression for  $\mathcal{I}$ , the vector  $\mathcal{J}$  defined in Equation (10) can be written as we can write

$$\mathcal{J}(\mathbf{r}, x) = \Lambda[\mathcal{S}(\mathbf{r}, x)]. \quad (26)$$

The source vector is given by

$$\mathcal{S}(\mathbf{r}, x) = p_x[\epsilon\mathcal{B}(\mathbf{r}) + \mathcal{J}(\mathbf{r}, x)] + (1 - p_x)\mathcal{S}_c(\mathbf{r}, x). \quad (27)$$

Substituting Equation (26) in Equation (27), we obtain a system of equations

$$[\hat{I} - p_x\Lambda]\mathcal{S}(\mathbf{r}, x) = p_x\epsilon\mathcal{B}(\mathbf{r}) + (1 - p_x)\mathcal{S}_c(\mathbf{r}, x), \quad (28)$$

which can be expressed in a symbolic form as

$$\hat{A}\mathcal{S} = \mathbf{b}. \quad (29)$$

The computing algorithm is given below:

Step (a): Let  $\hat{M}$  denote a preconditioner matrix (defined below). We introduce the 4-component initial preconditioned residual vectors  $\zeta_0$ ,  $\zeta_0^*$  and conjugate direction vectors  $\mathbf{p}_0$ . We define  $\zeta_0$  by

$$\zeta_0 = \hat{M}^{-1}\mathbf{b} - \hat{M}^{-1}\hat{A}\mathcal{S}_0, \quad (30)$$

and impose

$$\zeta_0^* = \zeta_0, \quad \mathbf{p}_0 = \zeta_0. \quad (31)$$

Here  $\mathcal{S}_0$  is an initial guess for the source vector defined by  $\mathcal{S}_0 = p_x\epsilon\mathcal{B} + (1 - p_x)\mathcal{S}_c$ . As we discretize the frequency and depths, the 4-component irreducible source vector and all the auxiliary vectors introduced in this algorithm can be treated as vectors of length  $4 \times n_x \times n_Y \times n_Z$ , where  $n_x$ ,  $n_Y$  and  $n_Z$  are the number of grid points in frequency,  $Y$  and  $Z$  co-ordinates respectively. The iterations are referred to by an index  $j$ , with  $j = 0, 1, 2, \dots$  *niter*, where *niter* is the number of iterations needed for convergence. For the  $j$ th iteration, the following steps are carried out.

Step (b): We use the formal solver to compute  $\hat{A}\mathbf{p}_j$ .

Step (c): We introduce a coefficient  $\alpha_j$  defined by

$$\alpha_j = \frac{\langle \zeta_j, \zeta_0^* \rangle}{\langle \hat{M}^{-1}\hat{A}\mathbf{p}_j, \zeta_0^* \rangle}. \quad (32)$$

where the angle brackets  $\langle \cdot, \cdot \rangle$  represent the inner product in the Euclidian space of real numbers  $\mathbb{R}^n$ , where  $n = 4 \times n_x \times n_Y \times n_Z$ .

Step (d): We introduce a new vector  $\mathbf{q}_j$  defined as

$$\mathbf{q}_j = \zeta_j - \alpha_j\hat{M}^{-1}\hat{A}\mathbf{p}_j. \quad (33)$$

Step (e): We use the formal solver to compute  $\hat{A}\mathbf{q}_j$ .

Step (f): We introduce a coefficient  $\omega_j$  defined by

$$\omega_j = \frac{\langle \hat{M}^{-1}\hat{A}\mathbf{q}_j, \mathbf{q}_j \rangle}{\langle \hat{M}^{-1}\hat{A}\mathbf{q}_j, \hat{M}^{-1}\hat{A}\mathbf{q}_j \rangle}. \quad (34)$$

Step (g): The value of the new irreducible source vector is derived from the recursive relation

$$\mathcal{S}_{j+1} = \mathcal{S}_j + \alpha_j\mathbf{p}_j + \omega_j\mathbf{q}_j. \quad (35)$$

Step (h): New values for the residual vectors  $\zeta_j$  and conjugate direction vectors  $\mathbf{p}_j$  are calculated with the recursive relations

$$\zeta_{j+1} = \mathbf{q}_j - \omega_j\hat{M}^{-1}\hat{A}\mathbf{q}_j, \quad (36)$$

$$\mathbf{p}_{j+1} = \zeta_{j+1} + \beta_j(\mathbf{p}_j - \omega_j\hat{M}^{-1}\hat{A}\mathbf{p}_j). \quad (37)$$

Here, the coefficient  $\beta_j$  is defined as

$$\beta_j = \frac{\langle \zeta_{j+1}, \zeta_0^* \rangle}{\langle \zeta_j, \zeta_0^* \rangle} \frac{\alpha_j}{\omega_j}. \quad (38)$$

Step (i): If the test for convergence described below is satisfied, we terminate the iteration sequence. Otherwise, we go to the Step (b).

*Test for Convergence:* At each iteration, we calculate the quantities

$$e_S = \max_{\tau_Y, \tau_Z, x=0} \{ |\delta S_0^0 / S_0^0| \} \quad (39)$$

which denotes the maximum relative change (MRC) on the first component  $S_0^0$  of the irreducible source vector and

$$e_P = \max_{\tau_Y, x=0, \theta_1, \varphi_1} \{ |\delta P / P| \} (\tau_Z = 0) \quad (40)$$

$$\text{with } P = \sqrt{(Q/I)^2 + (U/I)^2}, \quad (41)$$

which defines a maximum relative change on the surface polarization. The values of  $\theta_1$  and  $\varphi_1$  are given in Table 1. The test for convergence is defined as  $e \equiv \max[e_S, e_P] \leq \bar{\omega}$ , with  $\bar{\omega}$ , a given number. In this paper we use  $\bar{\omega} = 10^{-8}$ .

### The Preconditioner matrix

The preconditioner matrix  $\hat{M}$  is any form of implicit or explicit modification of the matrix  $\hat{A}$ , that helps to solve the given system of equations more efficiently (see Saad 2000). In a way, construction of the preconditioner matrix is similar to the construction of  $\Lambda^*$  matrix in ALI methods. For problems with CRD, the  $\hat{M}$  matrix is nothing but the diagonal matrix  $[\hat{I} - (1 - \epsilon)\Lambda^*]$ , with  $\Lambda^*$  being the diagonal of the  $\Lambda$  matrix. For problems with PRD, the kernel in the scattering integral has dependence on both  $x$  and  $x'$  and a diagonal preconditioner is not sufficient to represent this  $x, x'$  dependence. Therefore, we construct a preconditioner matrix  $\hat{M}$  given by

$$\hat{M} = [\hat{I} - (\hat{R}(x, x')/\phi(x))\Lambda_{x'}^*]. \quad (42)$$

It is a block diagonal matrix. Each block is a full matrix with respect to  $x$  and  $x'$ . The matrix  $\hat{M}$  is diagonal with respect to other variables. The  $\Lambda_x^*$  matrix in Equation (42) is constructed following the method of constructing the  $\Lambda_x^*$  matrix in the frequency by frequency (FBF) method of Paletou & Auer (1995).

Figure 4 demonstrates the performance of Pre-BiCG-STAB method in comparison to the Jacobi method. The model parameters chosen are same as those in Figure 5. We show progress of the maximum relative corrections  $e_S$  and  $e_P$  as a function of iteration number for these two methods. While the Jacobi method takes 186 iterations, Pre-BiCG-STAB takes only 26 iterations to reach the same level of accuracy ( $\bar{\omega} = 10^{-8}$ ). In terms of CPU time taken for the computations, the Pre-BiCG-STAB is much faster than the Jacobi method.

## 6. Results and Discussions

The numerical calculations have been performed with the irreducible Stokes and the source vectors. Most of the results presented in this section are for the Stokes parameters  $I, Q, U$  and the Stokes source vector components  $S_I, S_Q, S_U$  which are related to the irreducible components by

Equations (A1), (A2), and (A3). Figures 5 and 6 show the optical depth dependence of  $S_I, S_Q$  and  $S_U$  along the mid-axes in the  $Y$  and  $Z$  directions respectively, for two different frequencies namely  $x = 0$  and  $x = 5$ . The optical thickness in  $Y$  and  $Z$  directions are  $T_Y = T_Z = 2 \times 10^6$ . The damping parameter of the Voigt profile is  $a = 10^{-3}$ . We consider the pure line case ( $\kappa_c = 0$ ), with scattering according to PRD. The elastic and inelastic collision rates are respectively  $\Gamma_E/\Gamma_R = 10^{-4}$ ,  $\Gamma_I/\Gamma_R = 10^{-4}$ . The corresponding branching ratios are  $(\alpha, \beta^{(0)}, \beta^{(2)}) \approx (1, 1, 1)$ . This PRD model is dominated by the  $r_{II}$  redistribution function. The internal thermal sources are taken as constant (the Planck function  $B(\mathbf{r}) = 1$ ). The medium is assumed to be self-emitting (no incident radiation on the boundaries). We have plotted the results for all the 96 ( $= 12 \times 8$ ) directions that we have considered, which cover all the octants, with 12 directions per octant. For the first octant, they are listed in Table 1.

Figures 5(a) and (b) show the variation of source vectors along the mid  $Z$ -axis for  $x = 0$  and  $x = 5$  respectively. Because the  $Z$ -axis is the axis of symmetry,  $S_Q$  depends only on  $|\mu|$ , and hence only 4 out of 96 curves are distinguishable. For the same reason,  $S_U = 0$ .

Depth variation of the source vectors along the mid  $Y$ -axis is shown in Figures 6(a) and (b). Along the  $Y$ -axis,  $S_Q$  and  $S_U$  are sensitive to both  $\mu$  and  $\varphi$ . They show some symmetries which follow from the symmetry of the angle-gridding. For  $S_Q$ , the distinguishable curves correspond to the directions of the first octant. For  $S_U$ , the distinguishable curves correspond to all the directions in the first and second octants (second octant is defined by  $\theta \in [0, \pi/2], \varphi \in [\pi/2, \pi]$ ). Curves for the remaining directions coincide with these curves.

In Figures 5(b) and 6(b),  $S_Q$  and  $S_U$  are independent of the optical depth on the surface up to  $\tau = 10^4$  because, the monochromatic optical depth at  $x = 5$  is so small that the radiative transfer effects become negligible. The magnitudes of  $S_Q$  and  $S_U$  profiles are larger for  $x = 5$  because of the frequency coherent nature of  $r_{II}$  in the wings. When the thermalization has taken place,  $S_I \rightarrow B(\mathbf{r})$  and  $S_Q$  and  $S_U$  vanish. For  $x = 0$  this occurs at  $\tau \approx 10^4$  and for  $x = 5$  at  $\tau \approx 10^6$  (see Figures 5 and 6).

The angular behavior and sign changes of  $S_Q$

and  $S_U$  depend on the nature of the mean intensity components  $J_0^0$ ,  $J_0^2$ ,  $J_1^{2,y}$  and  $J_2^{2,x}$ . The behaviors of all these 4 components are controlled by the angular dependence of the intensity component  $I_0^0$ . Considering only the action of first column of the  $\hat{\Psi}$  matrix on  $I_0^0$ , these 4 components can be written as shown in Equation (B1). For example,  $J_0^2$  changes its sign roughly at the depth point where  $I_0^0$  changes its angular dependence from limb darkening (at the surface) to limb brightening (at the interior) (see Nagendra et al. 1998). The signs of other components depend on the  $\theta$  and  $\varphi$  dependence of  $I_0^0$  and on the signs of the trigonometric weights in each octant. For instance,  $J_1^{2,y}$  can be split into 8 terms, each representing the contribution from one octant. It can be easily seen that the trigonometric weights coming from four of these terms are positive ( $\theta \in [0, \pi/2]$  with  $\varphi \in [0, \pi/2], [\pi/2, \pi]$  and  $\theta \in [\pi/2, \pi]$  with  $\varphi \in [\pi, 3\pi/2], [3\pi/2, 2\pi]$ ). The weights for the remaining four terms are negative. If the sum of the positive terms dominates over the sum of the negative terms, then  $J_1^{2,y}$  will be positive, and vice-versa. This clearly shows that the signs of  $S_Q$  and  $S_U$  in a 2D medium depend strongly on the combined effects of  $\theta$  and  $\varphi$  dependence of the  $I_0^0$  component, unlike the 1D case, where  $I_0^0$  being independent of the azimuth, the sign of  $S_Q$  depends only on the  $\theta$  dependence of  $I_0^0$ .

In Figure 7 we show surface averaged emergent Stokes profiles for  $T = 2, 200$  and  $2 \times 10^6$ . By surface averaging, we mean that we integrate the values of the Stokes profiles in the  $Y$  direction at the surface ( $\tau_Z = 0$ ), by taking an arithmetic average. The other model parameters are same as in Figure 5. For both  $T = 2$  and  $200$ , the medium is effectively thin because  $\epsilon = 10^{-4}$ , and hence we see an emission line in the Stokes  $I$  profile. For  $T = 2 \times 10^6$  the medium is effectively thick, hence we see an emission line with self absorption in the core. Here the line core means that  $x \lesssim 4$ . Due to symmetries in the distribution of the angular quadrature points there are only 3 different curves for  $Q/I$  and only 6 different ones for  $U/I$ , out of the 12 azimuths. For effectively thin cases ( $T = 2, 200$ ), the product  $aT$  is smaller than unity and therefore the radiative transfer effects are restricted to the line core (see Nagendra et al. 1998). Therefore the source functions  $S_Q$  and  $S_U$  depend on the ray direction only in the line core. They

tend to zero in the line wings. The same behavior is seen of course for emergent  $Q/I$  and  $U/I$ . For  $T = 2 \times 10^6$ ,  $S_Q$  and  $S_U$  are almost independent of the ray direction in the line core but show significant variation in the wings. This is because of the larger monochromatic optical depth in the line core leading to an increased number of scattering. For wing frequencies, the angular dependence of  $Q/I$  and  $U/I$  is significant because,  $S_Q$  and  $S_U$  show variation throughout the atmosphere as the thermalization is reached only near the mid slab (see Figures 5(b) and 6(b)).

The magnitudes of  $Q/I$  and  $U/I$  increase with  $T$ . For  $|Q/I|$  the largest values are always at the line center. Further, for  $T = 2 \times 10^6$ , we see a dip at  $x \approx 12$  and a second peak at  $x \approx 20$ . For  $|U/I|$  the situation is a bit more complicated. For  $T = 2, 200$  the values of  $|U/I|$  are largest in the line core. For  $T = 2 \times 10^6$ ,  $|U/I|$  is very small in the line core and reaches up to 15 % in the wings around  $x \approx 12$ . These results are not easy to interpret, as they represent the case of an unsaturated radiation field that prevails in 2D slabs with intermediate optical thickness.

In Figure 8, we compare the surface averaged components of  $\mathcal{I}$  for 1D and 2D geometries in a semi-infinite media ( $T_Y = T_Z = T = 2 \times 10^9$ ). The continuum opacity parameter is  $\kappa_c = 10^{-8}$ . We have shown the results for  $\mu = 0.11$  and  $\varphi = 59.9^\circ$ . The other model parameters are same as in Figure 5. The  $I_0^0$  component is larger for 1D than 2D due to the leaking of the radiation from the boundaries of the 2D slab. The component  $|I_0^2|_{1D}$  is larger than  $|I_0^2|_{2D}$  because of the surface averaging. It acts in 2 different ways. (1) The signs of  $I_0^2$  change along the  $Y$  direction (2) the largest values of  $I_0^2$  occurs in narrow regions near the boundaries of the 2D slab (see Paper 1). The components with the index  $Q = 1, 2$  are zero for 1D. For 2D geometry,  $I_1^{2,x}$  and  $I_2^{2,y}$  are zero. The components  $I_2^{2,x}$  and  $I_1^{2,y}$  have significant values which contribute to the differences between the  $Q/I$  and  $U/I$  in 1D and 2D geometries.

In Figure 9 we show surface averaged emergent Stokes profiles for CRD and PRD in a semi-infinite 2D medium ( $T_Y = T_Z = T = 2 \times 10^9$ ). We choose the same PRD model as in Figure 5. This PRD model is dominated by  $r_{II}$ . The other model parameters are same as in Figure 8. We show the corresponding 1D results for compari-

son. Figures 9(a) and (b) correspond to  $\epsilon = 10^{-4}$  and  $\epsilon = 10^{-8}$  respectively. The global behaviors of  $I$  and  $Q/I$  for CRD and PRD in a 2D semi-infinite medium, are similar to those of 1D. As expected, intensity and polarization profiles for CRD and PRD are identical in the line core. In the wings, the Stokes  $I$  for CRD reaches a constant value and becomes independent of frequency whereas for PRD it varies sharply with frequency and reaches the CRD value only in the far wings. Further details of the behavior of Stokes profiles in semi-infinite 1D media can be found in Faurobert (1988). Now we focus on the essential differences between 1D and 2D results.  $[I]_{2D}$  is smaller than  $[I]_{1D}$  throughout the line profile due to leaking of the radiation field near the boundaries of the 2D slab for both CRD and PRD. For CRD,  $Q/I$  approaches zero in the wings while PRD profiles are non-zero ( $Q/I$  can take both positive and negative values). For CRD, the effects of 2D geometry are not as significant as for PRD.

We remark that for both CRD and PRD, the curves for  $[Q/I]_{1D}$  remain below the curves for  $[Q/I]_{2D}$ . This can be understood by looking at the components of the irreducible Stokes vector  $\mathcal{I}$  plotted in Figure 8. Equation (A2) can be rewritten as

$$\begin{aligned} [Q(\mathbf{r}, \boldsymbol{\Omega}, x)]_{1D} &\simeq -a_1 \times [I_0^2]_{1D}, \\ [Q(\mathbf{r}, \boldsymbol{\Omega}, x)]_{2D} &\simeq -a_1 \times [I_0^2]_{2D} + a_c, \end{aligned} \quad (43)$$

where  $a_1$  depends on  $\mu$  and is same for both 1D and 2D cases. The quantity  $a_c$  depends on  $\mu$ ,  $\varphi$  and the components  $I_1^{2,y}$  and  $I_2^{2,x}$ . For  $\mu = 0.11$  and  $\varphi = 59.9^\circ$  considered for Figure 8,  $a_1$  and  $a_c$  are positive. As discussed above,  $|I_0^2|_{1D}$  is larger than  $|I_0^2|_{2D}$ . When  $[I_0^2]_{2D} > 0$ ,  $-a_1 \times [I_0^2]_{2D} > -a_1 \times [I_0^2]_{1D}$  and therefore the addition of  $a_c$  to  $-a_1 \times [I_0^2]_{2D}$  leads to  $|Q/I|_{2D} < |Q/I|_{1D}$ . When  $[I_0^2]_{2D} < 0$ ,  $-a_1 \times [I_0^2]_{2D} < -a_1 \times [I_0^2]_{1D}$ . In this case, the addition of  $a_c$  to  $-a_1 \times [I_0^2]_{2D}$  may lead to  $|Q/I|_{2D} > |Q/I|_{1D}$  or  $|Q/I|_{2D} < |Q/I|_{1D}$ . But the contribution from  $a_c$  is sufficiently large that we have  $|Q/I|_{2D} > |Q/I|_{1D}$ . The differences between the  $[Q/I]_{2D}$  for other  $\varphi$  values and  $[Q/I]_{1D}$  are similar.

Finally, as pointed out in Paper 1,  $[U/I]_{2D}$  is non-zero and can become significantly large in the wings for the PRD case. In the CRD case  $[U/I]_{2D}$  is non-zero only very close to the line center and goes to zero in the rest of the frequency domain.

As is well known,  $[U/I]_{1D} \equiv 0$  due to axial symmetry.

## 7. Conclusions

In this paper we develop an efficient method to solve polarized radiative transfer equation with PRD in a 2D slab. We assume a two-level atom model with unpolarized ground level. We assume that the medium is finite in two directions ( $Y$  and  $Z$ ) and infinite in the third direction ( $X$ ). First we apply the Stokes vector decomposition technique developed in Paper 1 to 2D geometry. We show that due to symmetry of the Stokes  $I$  parameter with respect to the  $\varphi = \pi/2$  axis, the Stokes  $Q$  becomes symmetric and the Stokes  $U$  becomes anti-symmetric about this axis ( $\varphi$  is measured from the infinite  $X$  direction anti-clockwise). Using this property we can represent the polarized radiation field by 4 irreducible components  $I_0^0$ ,  $I_0^2$ ,  $I_1^{2,y}$  and  $I_2^{2,x}$ . The Stokes source vectors are also decomposed into 4 irreducible components which are independent of the ray direction. Due to axial symmetry  $I_1^{2,y}$  and  $I_2^{2,x}$  are zero in 1D geometry.

This decomposition technique is interesting for the development of iterative methods. Here we describe a numerical method called the Stabilized Preconditioned Bi-Conjugate Gradient (Pre-BiCG-STAB) and show that it is much faster than the Jacobi iteration method used in Paper 1. This method can be easily generalized to 3D geometries.

Further, in this paper we generalize to PRD, the 2D short characteristics method developed in Paletou et al. (1999) for CRD. This formal solver is much more efficient than the one used in Paper 1.

With these two new features it is possible to compute the solutions for a wide range of model parameters. With the method of Paper 1 only media with small optical depths can be considered.

In Figure 5 and 6 we show the optical depth dependence of the source vectors along the mid axes in the  $Y$  and  $Z$  directions. We recover similar angular dependence of  $S_Q$  and  $S_U$  at line center as in Paletou et al. (1999). Contrary to CRD, one can observe the increase in the values of  $S_Q$  and  $S_U$  at  $x = 5$ . This is a PRD effect on the polarization caused by the coherence nature of  $r_{II}$  redistribution function in the wings.

In Figure 7 we study the surface averaged emergent Stokes profiles for different optical thicknesses. We show that the polarization is restricted to the line core for small values of  $T$ . As  $T$  increases,  $Q/I, U/I$  take larger values in the line wings as well. This is also a PRD effect. In the line core  $Q/I$  becomes independent of the ray directions and  $U/I \rightarrow 0$  due to an increased number of scattering for the line core photons.

In Figures 8 and 9 we consider the case of semi-infinite atmospheres with  $T_Z = T_Y = T = 2 \times 10^9$ . In Figure 8 we compare the behaviors of the emergent irreducible components averaged over the surface, for 2D geometry and the corresponding components in 1D geometry. For 1D geometry only non-zero components are  $I_0^0$  and  $I_0^2$ . The  $I_0^0$  component is larger for 1D than 2D due to the leaking of the radiation from the boundaries of the 2D slab. The component  $|I_0^2|_{1D}$  is larger than  $|I_0^2|_{2D}$  due to surface averaging. The contribution from the components  $I_2^{2,x}$  and  $I_1^{2,y}$  is mainly responsible for the deviation of  $Q/I$  and  $U/I$  in 2D geometry from their 1D values.

In Figure 9 we compare the surface averaged emergent Stokes profiles in 2D geometry, and the corresponding 1D solutions for CRD and PRD. We show that the deviation of polarized radiation field in 2D geometry from the one in 1D geometry exists both for CRD and PRD, but is more severe in the line wings of the PRD solutions. In Figure 9(a), at  $x \approx 12$ , we see a near wing maxima in  $-[Q/I]$ . At this frequency  $||Q/I|_{2D} - |Q/I|_{1D}| \approx 2\%$ . At this wing frequency we have  $|U/I|_{2D} \approx 3\%$  and  $|U/I|_{1D} \equiv 0$ .

We thus propose our numerical method as an efficient and fast method to solve the polarized radiative transfer problems with PRD in multi-dimensional media.

We are grateful to Prof. H. Frisch for critical reading of the manuscript and very useful suggestions which greatly helped to improve the paper. We thank Dr. Sampoorna for helpful discussions.

### A. Expansion of Stokes parameters into irreducible components

The Stokes parameters and the irreducible Stokes vector are related through the following expressions. They are already given in Frisch (2007). However we present these expressions here for an easy reference. The expressions given below are applicable for radiative transfer in 2D geometry (see Equation (14) and discussions that follows).

$$\begin{aligned}
 I(\mathbf{r}, \boldsymbol{\Omega}, x) &= I_0^0 + \frac{1}{2\sqrt{2}}(3 \cos^2 \theta - 1)I_0^2 \\
 &+ \sqrt{3} \cos \theta \sin \theta \sin \varphi I_1^{2,y} + \frac{\sqrt{3}}{2}(1 - \cos^2 \theta) \cos 2\varphi I_2^{2,x},
 \end{aligned} \tag{A1}$$

$$\begin{aligned}
 Q(\mathbf{r}, \boldsymbol{\Omega}, x) &= -\frac{3}{2\sqrt{2}}(1 - \cos^2 \theta)I_0^2 \\
 &+ \sqrt{3} \cos \theta \sin \theta \sin \varphi I_1^{2,y} - \frac{\sqrt{3}}{2}(1 + \cos^2 \theta) \cos 2\varphi I_2^{2,x},
 \end{aligned} \tag{A2}$$

$$U(\mathbf{r}, \boldsymbol{\Omega}, x) = \sqrt{3} \sin \theta \cos \varphi I_1^{2,y} + \sqrt{3} \cos \theta \sin 2\varphi I_2^{2,x}. \tag{A3}$$

The irreducible components in the above equations depend on  $\mathbf{r}$ ,  $\boldsymbol{\Omega}$  and  $x$ . The same transformation formulas can be used to construct the Stokes source vectors from the irreducible source vectors.

### B. Symmetry of polarized radiation field in 2D geometries

Equation (14) concerns symmetry of polarized radiation field in 2D geometries. A proof of Equation (14) can be given as an algorithm.

Step (1): First we assume that the medium has only an unpolarized thermal source namely,  $\mathcal{S}(\mathbf{r}, x) = (\epsilon B(\mathbf{r}), 0, 0, 0, 0, 0)^T$ .

Step (2): Use of this source vector in the formal solution expression (Equation 23) yields  $\mathcal{I} = (I_0^0, 0, 0, 0, 0, 0)^T$ .

Step 3: Using this  $\mathcal{I}$ , we can write the expressions for the irreducible mean intensity components as

$$\begin{aligned}
J_0^0(\mathbf{r}, x) &\simeq \int_{x', \Omega} \frac{\hat{R}(x, x')}{\phi(x)} I_0^0(\mathbf{r}, \theta, \varphi, x), \\
J_0^2(\mathbf{r}, x) &\simeq c_2 \int_{x', \Omega} \frac{\hat{R}(x, x')}{\phi(x)} (3 \cos^2 \theta - 1) I_0^0(\mathbf{r}, \theta, \varphi, x), \\
J_1^{2,x}(\mathbf{r}, x) &\simeq -c_3 \int_{x', \Omega} \frac{\hat{R}(x, x')}{\phi(x)} \sin 2\theta \cos \varphi I_0^0(\mathbf{r}, \theta, \varphi, x), \\
J_1^{2,y}(\mathbf{r}, x) &\simeq c_4 \int_{x', \Omega} \frac{\hat{R}(x, x')}{\phi(x)} \sin 2\theta \sin \varphi I_0^0(\mathbf{r}, \theta, \varphi, x), \\
J_2^{2,x}(\mathbf{r}, x) &\simeq c_5 \int_{x', \Omega} \frac{\hat{R}(x, x')}{\phi(x)} \sin^2 \theta \cos 2\varphi I_0^0(\mathbf{r}, \theta, \varphi, x), \\
J_2^{2,y}(\mathbf{r}, x) &\simeq -c_6 \int_{x', \Omega} \frac{\hat{R}(x, x')}{\phi(x)} \sin^2 \theta \sin 2\varphi I_0^0(\mathbf{r}, \theta, \varphi, x),
\end{aligned} \tag{B1}$$

where

$$\int_{x', \Omega} = \int_{-\infty}^{+\infty} dx' \oint \frac{d\Omega}{4\pi}, \tag{B2}$$

and  $c_i, i = 2, 3, 4, 5, 6$  are positive numbers (see appendix A of Paper 1). We recall that  $d\Omega = \sin \theta d\theta d\varphi$ ,  $\theta \in [0, \pi]$  and  $\varphi \in [0, 2\pi]$ .

Step 4: Notice that  $\cos(\pi - \varphi) = -\cos \varphi$ ,  $\sin 2(\pi - \varphi) = -\sin 2\varphi$ .

Step 5: Using the formal solution computed with the thermal source vector  $(\epsilon B(\mathbf{r}), 0, 0, 0, 0, 0)^T$ , and the fact that in a 2D geometry, the medium is homogeneous in the  $X$  direction, it follows that

$$\begin{aligned}
I_0^0(\mathbf{r}, \theta, \varphi, x') &= I_0^0(\mathbf{r}, \theta, \pi - \varphi, x'), \\
I_0^0(\mathbf{r}, \theta, \pi + \varphi, x') &= I_0^0(\mathbf{r}, \theta, 2\pi - \varphi, x'), \quad \varphi \in [0, \pi/2].
\end{aligned} \tag{B3}$$

Step 6: Substituting Equation (B3) in Equation (B1), we can easily prove that

$$\begin{aligned}
(J_1^{2,x})^{(1)} &= 0, (J_2^{2,y})^{(1)} = 0, \\
\text{and hence} \\
(S_1^{2,x})^{(1)} &= 0, (S_2^{2,y})^{(1)} = 0,
\end{aligned} \tag{B4}$$

where the superscript (1) means that it is a first order solution.

Step 7: Using Equation (B4), along with Equations (A1), (A2) and (A3) applied to the source vectors we deduce

$$\begin{aligned}
S_I(\mathbf{r}, \theta, \varphi, x) &= S_I(\mathbf{r}, \theta, \pi - \varphi, x), \\
S_I(\mathbf{r}, \theta, \varphi + \pi, x) &= S_I(\mathbf{r}, \theta, 2\pi - \varphi, x), \\
S_Q(\mathbf{r}, \theta, \varphi, x) &= S_Q(\mathbf{r}, \theta, \pi - \varphi, x), \\
S_Q(\mathbf{r}, \theta, \varphi + \pi, x) &= S_Q(\mathbf{r}, \theta, 2\pi - \varphi, x), \\
S_U(\mathbf{r}, \theta, \varphi, x) &= -S_U(\mathbf{r}, \theta, \pi - \varphi, x), \\
S_U(\mathbf{r}, \theta, \varphi + \pi, x) &= -S_U(\mathbf{r}, \theta, 2\pi - \varphi, x).
\end{aligned} \tag{B5}$$

Step 8: Using formal solution for Stokes parameters  $I, Q, U$  and using the homogeneity of the 2D slab in the  $X$  direction, it follows that

$$\begin{aligned}
I(\mathbf{r}, \theta, \varphi, x) &= I(\mathbf{r}, \theta, \pi - \varphi, x), \\
I(\mathbf{r}, \theta, \varphi + \pi, x) &= I(\mathbf{r}, \theta, 2\pi - \varphi, x), \\
Q(\mathbf{r}, \theta, \varphi, x) &= Q(\mathbf{r}, \theta, \pi - \varphi, x), \\
Q(\mathbf{r}, \theta, \varphi + \pi, x) &= Q(\mathbf{r}, \theta, 2\pi - \varphi, x), \\
U(\mathbf{r}, \theta, \varphi, x) &= -U(\mathbf{r}, \theta, \pi - \varphi, x), \\
U(\mathbf{r}, \theta, \varphi + \pi, x) &= -U(\mathbf{r}, \theta, 2\pi - \varphi, x).
\end{aligned} \tag{B6}$$

Step 9: Now we recall the expression for the complex irreducible source vector components  $S_{Q,l}^K$  (see Equation (14) in Paper 1 and Equation (20) for zero magnetic field case in Frisch (2007)) namely,

$$S_{Q,l}^K(\mathbf{r}, x) = G_Q^K(\mathbf{r}, x) + J_Q^K(\mathbf{r}, x), \tag{B7}$$

where

$$\begin{aligned}
J_Q^K(\mathbf{r}, x) &= \frac{1}{\phi(x)} \int_{-\infty}^{+\infty} dx' \oint \frac{d\Omega}{4\pi} \\
&\times R^K(x, x') \sum_{j=0}^3 (-1)^Q \mathcal{T}_{-Q}^K(j, \Omega) I_j(\mathbf{r}, \Omega, x').
\end{aligned} \tag{B8}$$

Here  $I_0, I_1, I_2=I, Q, U$ . The quantity  $R^{(0)}(x, x')$  is the first element of the matrix  $\hat{R}$ . All the other elements are given by  $R^{(2)}(x, x')$ .

Step 10: We consider the case  $K = 2, Q = 1$ . Substituting the expressions for  $\mathcal{T}_{-Q}^K(j, \Omega)$  from Landi Degl'Innocenti & Landolfi (2004) for the reference direction  $\gamma = 0$ , the integral over  $\varphi$  in Equation (B8) can be written as

$$\begin{aligned}
\int_0^{2\pi} d\varphi \sum_{j=0}^3 (\mathcal{T}_1^2)^*(j, \Omega) I_j(\mathbf{r}, \Omega, x') &= \int_0^{2\pi} d\varphi \left[ (\mathcal{T}_1^2)^*(0, \theta, \varphi) I(\mathbf{r}, \theta, \varphi, x') \right. \\
&\left. + (\mathcal{T}_1^2)^*(1, \theta, \varphi) Q(\mathbf{r}, \theta, \varphi, x') + (\mathcal{T}_1^2)^*(2, \theta, \varphi) U(\mathbf{r}, \theta, \varphi, x') \right].
\end{aligned} \tag{B9}$$

Step 11: The  $\varphi$  integral in Equation (B9) can be split into 2 parts, one from 0 to  $\pi$  and the other from  $\pi$  to  $2\pi$ . It can be shown that both these integrals yield purely imaginary functions. First we consider the integral from 0 to  $\pi$  and decompose into integrals over 0 to  $\pi/2$  and  $\pi/2$  to  $\pi$ . In the integral from  $\pi/2$  to  $\pi$

we perform a change of variable  $\varphi \rightarrow \pi - \varphi$ . We obtain

$$\begin{aligned}
& \int_0^\pi d\varphi \sum_{j=0}^3 (\mathcal{T}_1^2)^*(j, \boldsymbol{\Omega}) I_j(\mathbf{r}, \boldsymbol{\Omega}, x') \\
&= \int_0^{\pi/2} d\varphi \left[ (\mathcal{T}_1^2)^*(0, \theta, \varphi) + (\mathcal{T}_1^2)^*(0, \theta, \pi - \varphi) \right] I(\mathbf{r}, \theta, \varphi, x') \\
&+ \left[ (\mathcal{T}_1^2)^*(1, \theta, \varphi) + (\mathcal{T}_1^2)^*(1, \theta, \pi - \varphi) \right] Q(\mathbf{r}, \theta, \varphi, x') \\
&+ \left[ (\mathcal{T}_2^2)^*(1, \theta, \varphi) - (\mathcal{T}_1^2)^*(2, \theta, \pi - \varphi) \right] U(\mathbf{r}, \theta, \varphi, x'), \\
&= \int_0^{\pi/2} d\varphi \left[ \frac{\sqrt{3}}{2} \sin \theta \cos \theta (-e^{-i\varphi} - e^{-i(\pi-\varphi)}) \right] I(\mathbf{r}, \theta, \varphi, x') \\
&+ \left[ \frac{\sqrt{3}}{2} \sin \theta \cos \theta (-e^{-i\varphi} - e^{-i(\pi-\varphi)}) \right] Q(\mathbf{r}, \theta, \varphi, x') \\
&+ \left[ \frac{\sqrt{3}}{2} i \sin \theta (e^{-i\varphi} - e^{-i(\pi-\varphi)}) \right] U(\mathbf{r}, \theta, \varphi, x') \\
&= \int_0^{\pi/2} d\varphi \left[ \frac{\sqrt{3}}{2} \sin \theta \cos \theta (2i \sin \varphi) \right] I(\mathbf{r}, \theta, \varphi, x') \\
&+ \left[ \frac{\sqrt{3}}{2} \sin \theta \cos \theta (2i \sin \varphi) \right] Q(\mathbf{r}, \theta, \varphi, x') \\
&+ \left[ \frac{\sqrt{3}}{2} i \sin \theta (2 \cos \varphi) \right] U(\mathbf{r}, \theta, \varphi, x'), \tag{B10}
\end{aligned}$$

which is purely an imaginary function. Similarly we can prove that the integral of  $\varphi$  from  $\pi$  to  $2\pi$  also yields a purely imaginary function. Thus  $J_1^2$  is purely imaginary. Since  $J_1^{2,x}$  is the real part of  $J_1^2$ , we have  $J_1^{2,x} = 0$ .

Following similar lines we can prove that  $J_2^2$  is purely real, which proves that  $J_2^{2,y} = 0$  where  $J_2^{2,y}$  is the imaginary part of  $J_2^2$ . Thus we get

$$(J_1^{2,x})^{(2)} = 0, (J_2^{2,y})^{(2)} = 0, \tag{B11}$$

and hence

$$(S_1^{2,x})^{(2)} = 0, (S_2^{2,y})^{(2)} = 0, \tag{B12}$$

where the subscript (2) means second order solution. Repeating the above steps (7)–(11), we can prove that Equations (B11) and (B12) are valid for any order  $n$ . Hence the proof.

## REFERENCES

- Adam, J. 1990, *A&A*, 240, 541
- Anusha, L. S., Nagendra, K. N., Paletou, F., & Léger, L. 2009, *ApJ*, 704, 661
- Anusha, L. S., & Nagendra, K. N. 2010, (submitted), Paper 1
- Auer, L. H., & Paletou, F. 1994, *A&A*, 285, 675
- Auer, L. H., Fabiani Bendicho, P., & Trujillo Bueno, J. 1994, *A&A*, 292, 599
- Bommier, V. 1997, *A&A*, 328, 726
- Carlsson, B. G. 1963, in *Methods in Computational Physics*, Vol 1, Academic Press, 1
- Dittmann, O. J. 1999, in *Solar Polarization*, ed. K. N. Nagendra & J. O. Stenflo (Boston: Kluwer), 201
- Domke, H., & Hubeny, I. 1988, *ApJ*, 334, 527
- Faurobert, M. 1988, *A&A*, 194, 268
- Faurobert-Scholl, M., 1992, *A&A*, 258, 521
- Folini, D. 1998, PhD Thesis, Institute of Astronomy, ETH Zurich, Switzerland
- Frisch, H. 2007, *A&A*, 476, 665
- Hillier, D. J. 1996, *A&A*, 308, 521
- Hubeny, I., & Burrows, A. 2007, *ApJ*, 659, 1458
- Hummer, D. G. 1962, *MNRAS*, 125, 21
- Klein, R. I., Castor, J. I., Greenbaum, A., Taylor, D., & Dykema, P. G. 1989, *JQSRT*, 41, 199
- Kunasz, P., & Auer, L. H. 1988, *JQSRT*, 39, 67
- Landi Degl'Innocenti, E., & Landolfi, M. 2004, *Polarization in Spectral Lines* (Dordrecht: Kluwer)
- Meinkohn, E. 2009, in *Numerical Methods in Multidimensional Radiative Transfer* ed. Kanschat, G., Meinkohn, E., Rannacher, R., & Wehrse, R. (Springer), 99
- Manso Sainz, R., & Trujillo Bueno, J. 1999, in *Solar Polarization*, ed. K. N. Nagendra & J. O. Stenflo (Boston: Kluwer), 143
- Mihalas, D., Auer, L. H., & Mihalas, B. R. 1978, *ApJ*, 220, 1001
- Nagendra, K. N., Frisch, H., & Faurobert-Scholl, M. 1998, *A&A*, 332, 610
- Nagendra, K. N., & Sampoorna, M. 2009, in *Solar Polarization*, eds. S. V. Berdyugina, K. N. Nagendra, & R. Ramelli (San Francisco: ASP), 261
- Nagendra, K. N., Anusha, L. S., & Sampoorna, M. 2009, in *3D Views on Cool Stellar atmospheres: Theory meets Observation*, ed. Nagendra, K. N., Bonifacio, P., & Ludwig, H.-G. *Memorie della Societa Astronomica Italiana*, 80
- Paletou, F., & Auer, L. H. 1995, *A&A*, 297, 771
- Paletou, F., Bommier, V., & Faurobert-Scholl, M. 1999, in *Solar Polarization*, ed. K. N. Nagendra & J. O. Stenflo (Boston: Kluwer), 189
- Paletou, F., & Anterrieu, E. 2009, *A&A*, 507, 1815
- Papkalla, R. 1995, *A&A*, 295, 551
- Saad, Y. 2000, *Iterative methods for Sparse Linear Systems* (2nd ed.) (ebook:<http://www-users.cs.umn.edu/saad/books.html>)
- Trujillo Bueno, J. 2003, in *Solar Polarization*, ed. J. Trujillo Bueno & J. Sánchez Almeida (San Francisco: ASP), 551

Table 1: The 12-point Carlsson type B angle points and weights for a quadrature of order  $n = 8$ . See Figure 3(b) for the definition of  $\theta$  and  $\varphi$ .

(a)

i	$\mu_i$	$\eta_i$	$\gamma_i$	$w_i$
1	0.857080E+00	0.111044E+00	0.503073E+00	0.142935E-01
2	0.702734E+00	0.111044E+00	0.702734E+00	0.992212E-02
3	0.503073E+00	0.111044E+00	0.857080E+00	0.142935E-01
4	0.857080E+00	0.503073E+00	0.111044E+00	0.142935E-01
5	0.702734E+00	0.503073E+00	0.503073E+00	0.315749E-02
6	0.503073E+00	0.503073E+00	0.702734E+00	0.315749E-02
7	0.111044E+00	0.503073E+00	0.857080E+00	0.142935E-01
8	0.702734E+00	0.702734E+00	0.111044E+00	0.992212E-02
9	0.503073E+00	0.702734E+00	0.503073E+00	0.315749E-02
10	0.111044E+00	0.702734E+00	0.702734E+00	0.992212E-02
11	0.503073E+00	0.857080E+00	0.111044E+00	0.142935E-01
12	0.111044E+00	0.857080E+00	0.503073E+00	0.142935E-01

(b)

i	$\theta_i$	$\varphi_i$
1	0.310097E+02	0.775526E+02
2	0.453533E+02	0.810205E+02
3	0.597965E+02	0.826178E+02
4	0.310097E+02	0.124474E+02
5	0.453533E+02	0.450000E+02
6	0.597965E+02	0.544019E+02
7	0.836245E+02	0.595887E+02
8	0.453533E+02	0.897951E+01
9	0.597965E+02	0.355981E+02
10	0.836245E+02	0.450000E+02
11	0.597965E+02	0.738219E+01
12	0.836245E+02	0.304113E+02

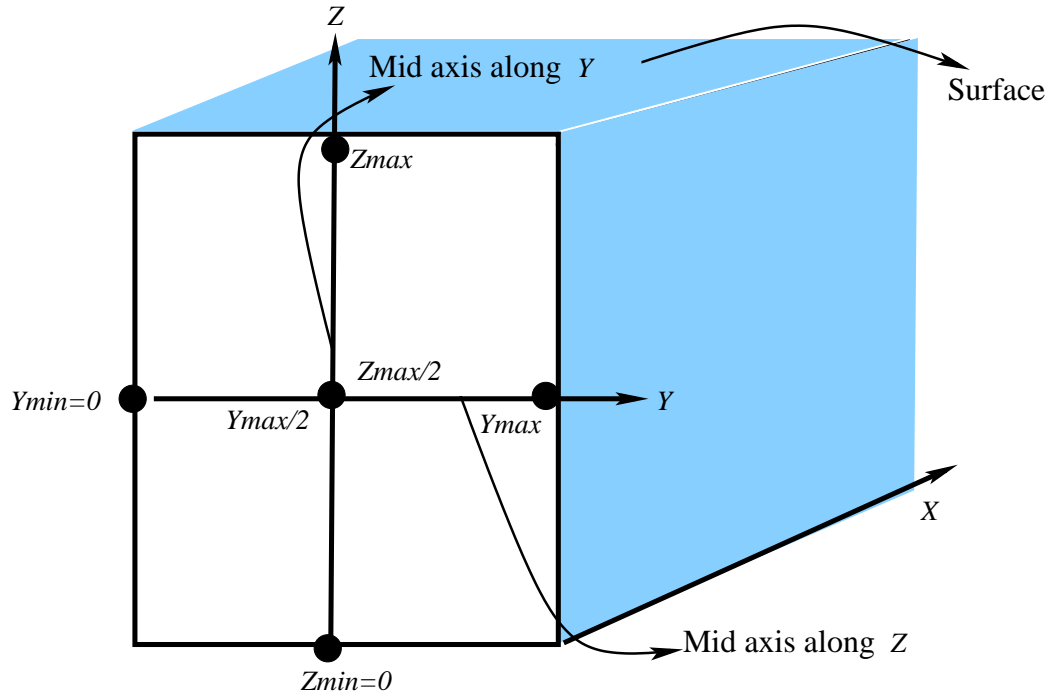


Fig. 1.— Figure showing the radiative transfer in 2D geometry. The medium is finite in  $Y$  and  $Z$  directions and infinite in the  $X$  direction. The mid-axes along  $Y$  and  $Z$  are marked. In Figures 5 and 6 the variation of the Stokes source vectors along these mid axes are shown.

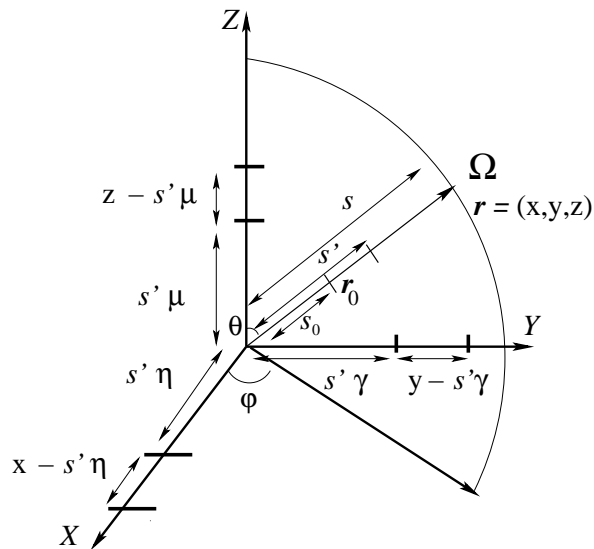


Fig. 2.— The definition of the spatial location  $\mathbf{r}$  and the projected distances  $\mathbf{r} - s'\boldsymbol{\Omega}$  which appear in the 2D formal solution integral.  $\mathbf{r}_0$  and  $\mathbf{r}$  are the arbitrary initial and final locations considered in the formal solution integral.

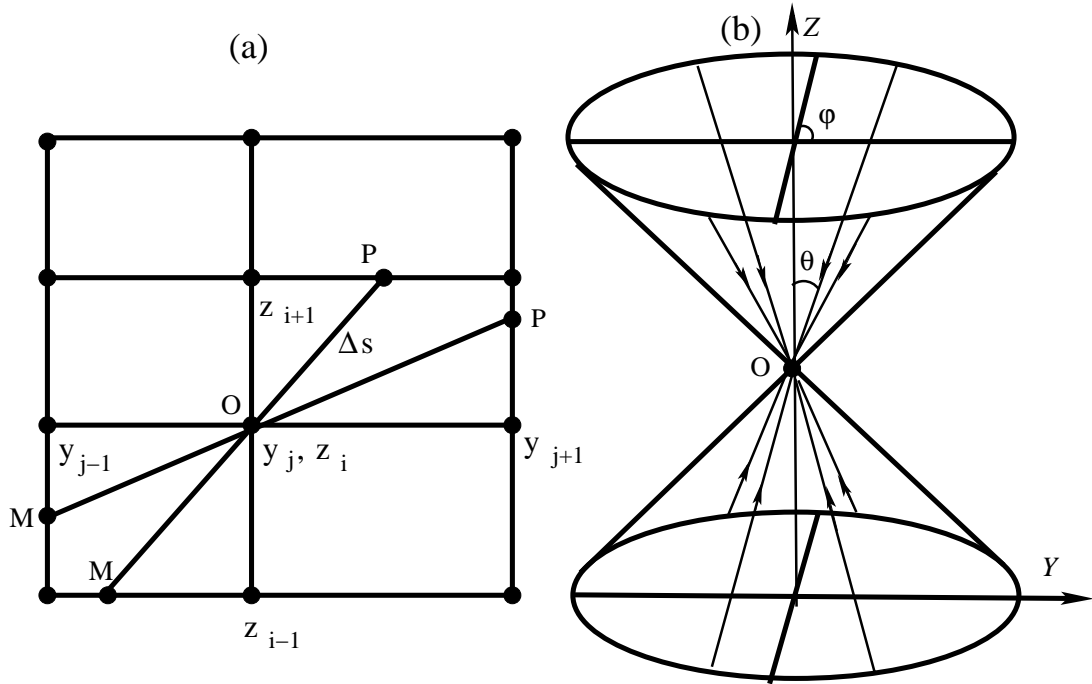


Fig. 3.— Figure showing the geometry of the 2D transfer problem. MOP in panel (a) represents a stencil of short characteristics along a ray path, after projecting the ray onto a 2D plane. The points used for the interpolation of  $\mathcal{S}$ ,  $\kappa_{tot}$  at M and P, and the upwind intensity  $\mathcal{I}_M$  are marked. In panel (b) we show all the rays in the  $4\pi$  steradians considered for computing the scattering integral, in the local co-ordinate system at O.

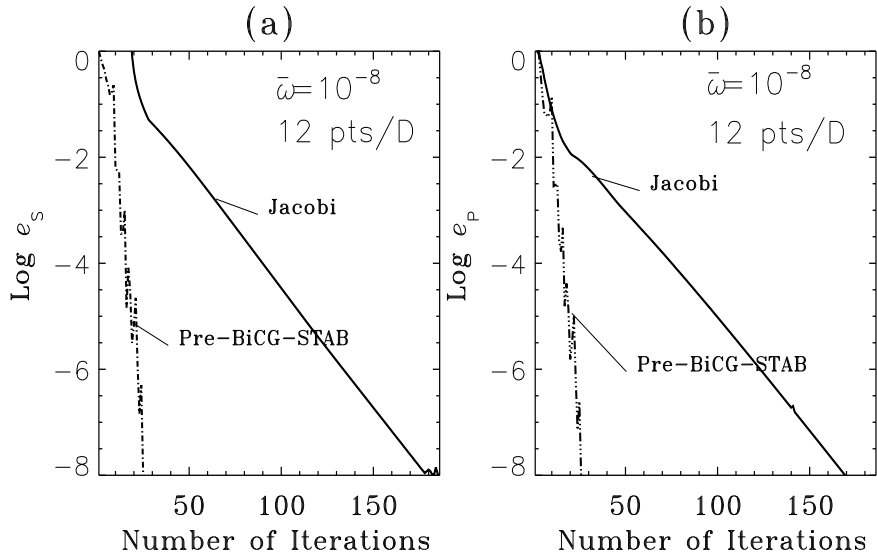


Fig. 4.— Figure showing the progress of maximum relative correction in the first component of the irreducible source vector ( $e_s$ ) and the surface polarization ( $e_p$ ) for Jacobi and Pre-BiCG-STAB methods. A convergence criteria of  $10^{-8}$  is used. Spatial gridding has 12 points per decade.

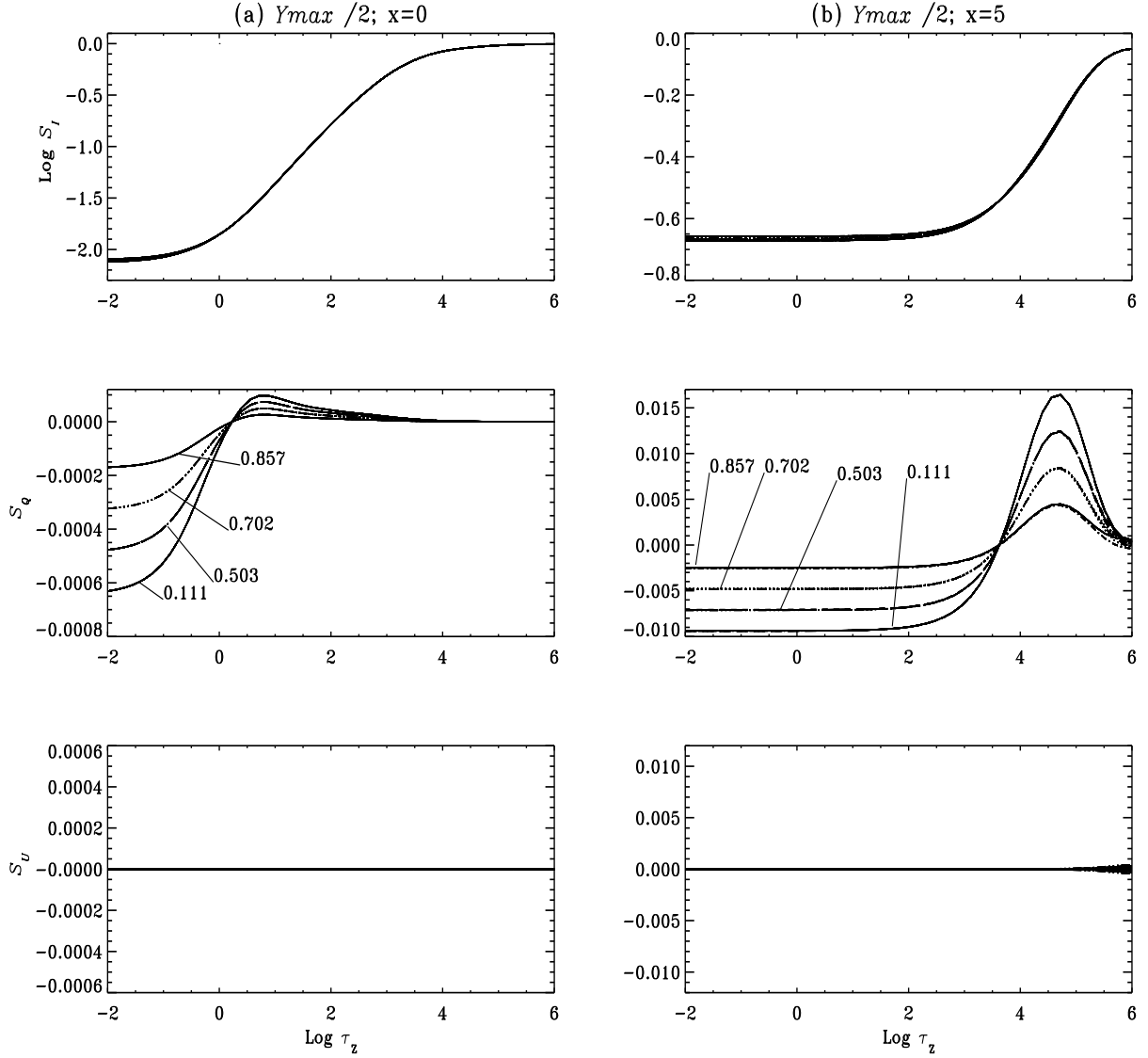


Fig. 5.— Variation of the Stokes source vectors as a function of optical depth. The model parameters are  $(T_Z, T_Y, a, \epsilon, \kappa_c, \Gamma_E/\Gamma_R) = (2 \times 10^6, 2 \times 10^6, 10^{-3}, 10^{-4}, 0, 10^{-4})$ . Panels (a) and (b) show variations of the source vectors along the  $Z$ -axis at  $Y_{max}/2$  for frequencies  $x = 0$  and  $x = 5$  respectively. The mid  $Y$ -axis is marked in Figure 1. The results are shown for a half slab only due to symmetry about the mid axes. The curves are labeled by the values of  $\mu$ .

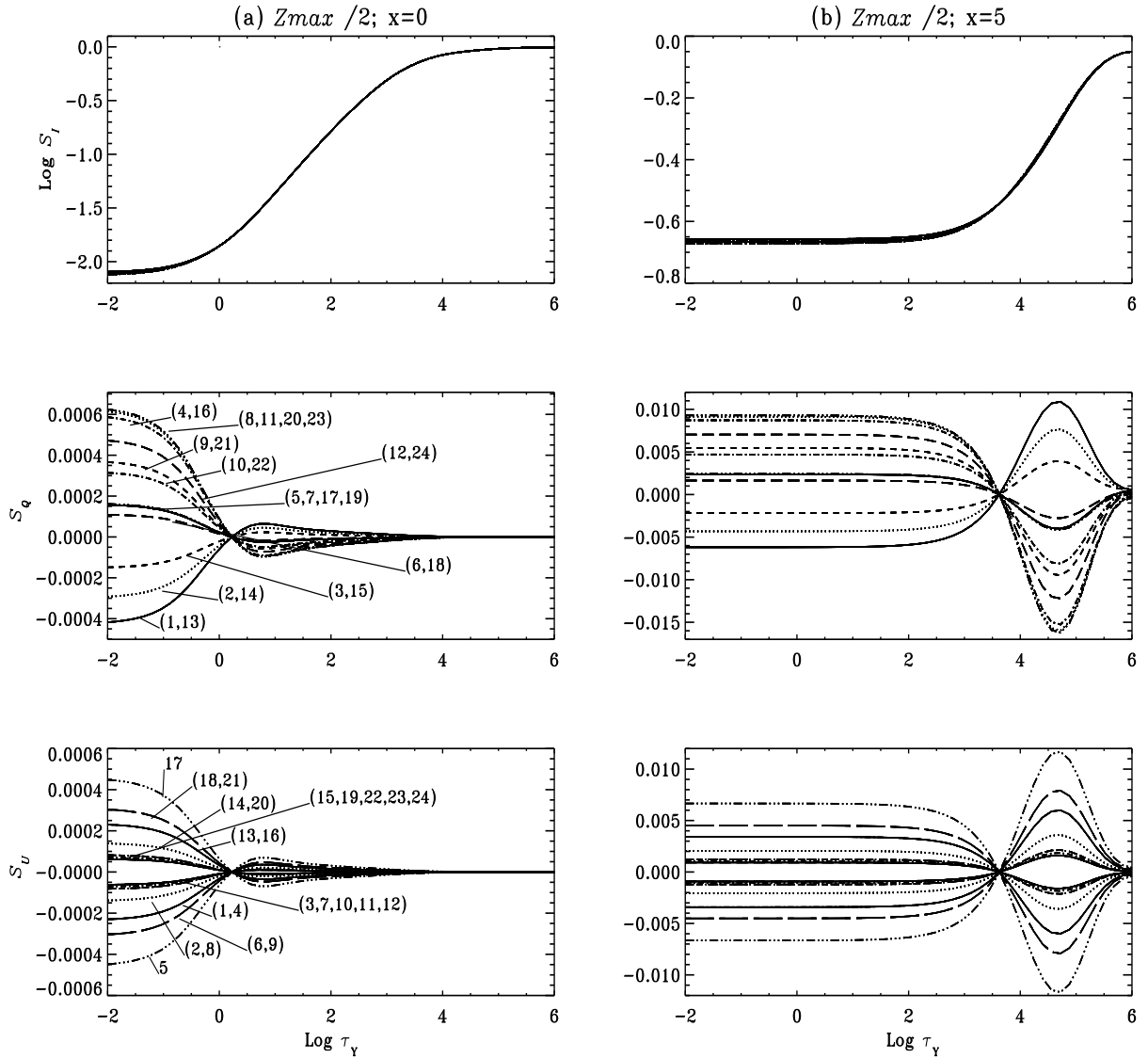


Fig. 6.— Same as Figure 5, but along the  $Y$ -axis at  $Z_{max}/2$ . The mid  $Z$ -axis is marked in Figure 1. The indices 1–12 near the curves refer to the indices of the directions for first octant given in Table 1. The indices 13–24 refer to the indices of the directions in the second octant. They can be computed easily using simple trigonometric relations. The labels for the curves in panel (b) are the same as those in panel (a) for the respective line types.

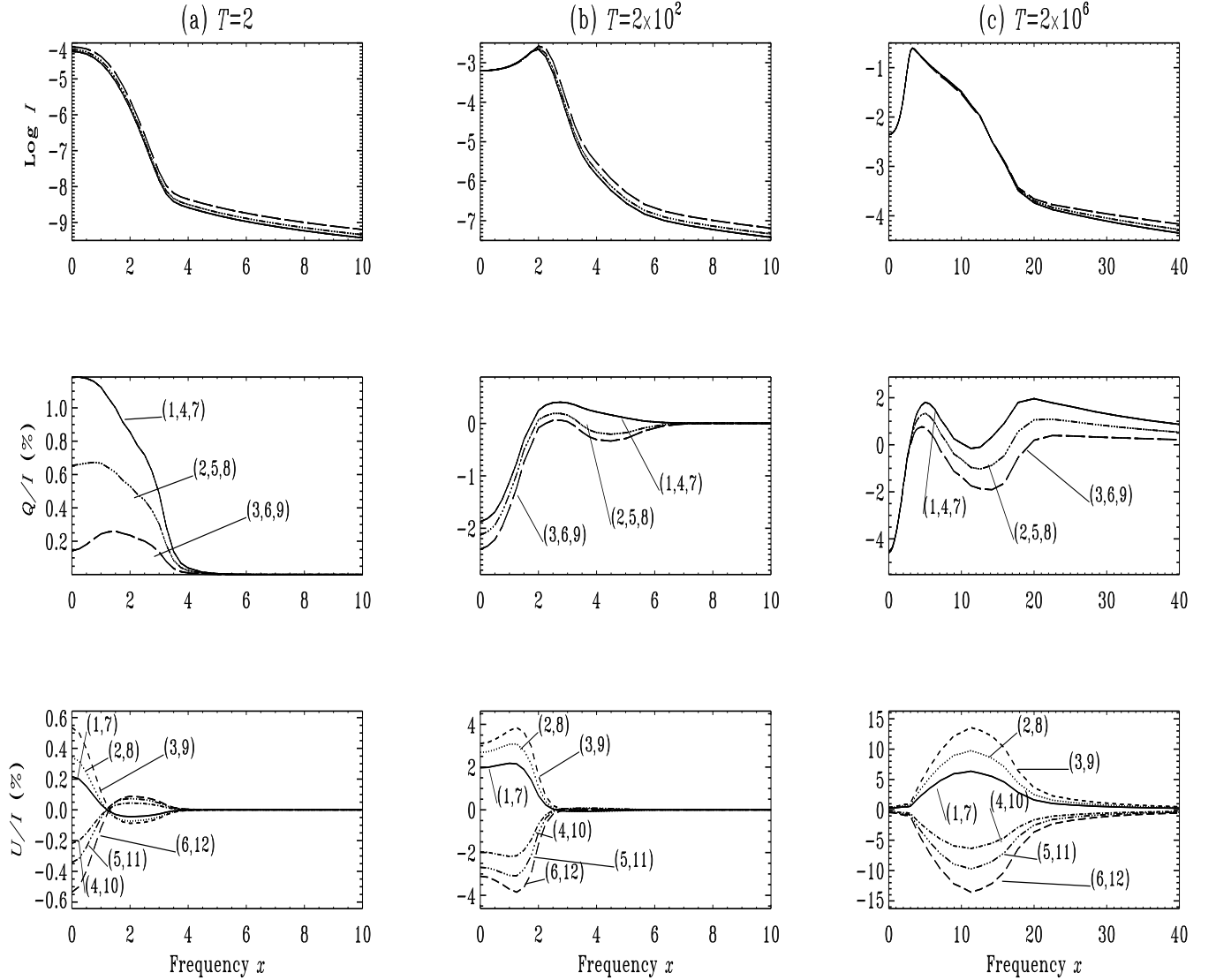


Fig. 7.— Optical depth effects on 2D polarized radiation field. The surface averaged emergent Stokes profiles are presented for  $T_Y = T_Z = T = 2, 200, 2 \times 10^6$ . The other model parameters are same as those in Figure 5. The results are plotted for 12 directions with  $\mu = 0.11$  and 12  $\varphi$  values given by  $\varphi_i (i = 1, 12) = 59.9, 44.9, 30.4, 300.4, 315, 329, 120.4, 135, 149.6, 239.6, 225, 210.4$ . First 3  $\varphi$  values correspond to first octant and are given in Table 1. The curves are labeled by the indices of  $\varphi$ . Due to symmetry reasons, only some of them are distinct.

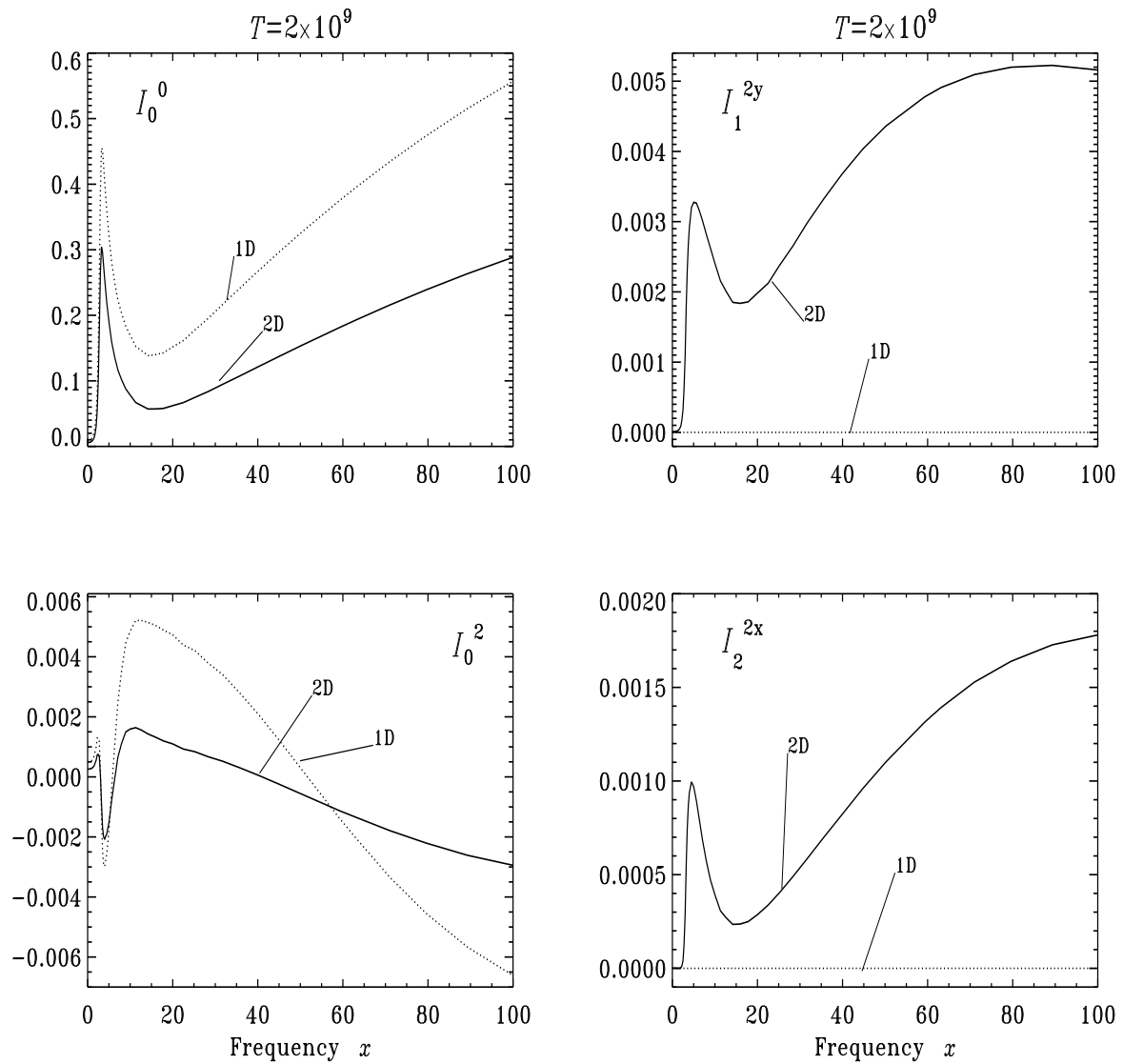


Fig. 8.— Comparison of the surface averaged components of irreducible Stokes vector  $\mathcal{I}$  in 1D and 2D semi-infinite media ( $T = T_Y = T_Z = 2 \times 10^9$ ). The results are shown for  $\mu = 0.11$  and  $\varphi = 59.9^\circ$ . The continuum opacity parameter  $\kappa_c = 10^{-8}$ . Other model parameters are same as those in Figure 5.

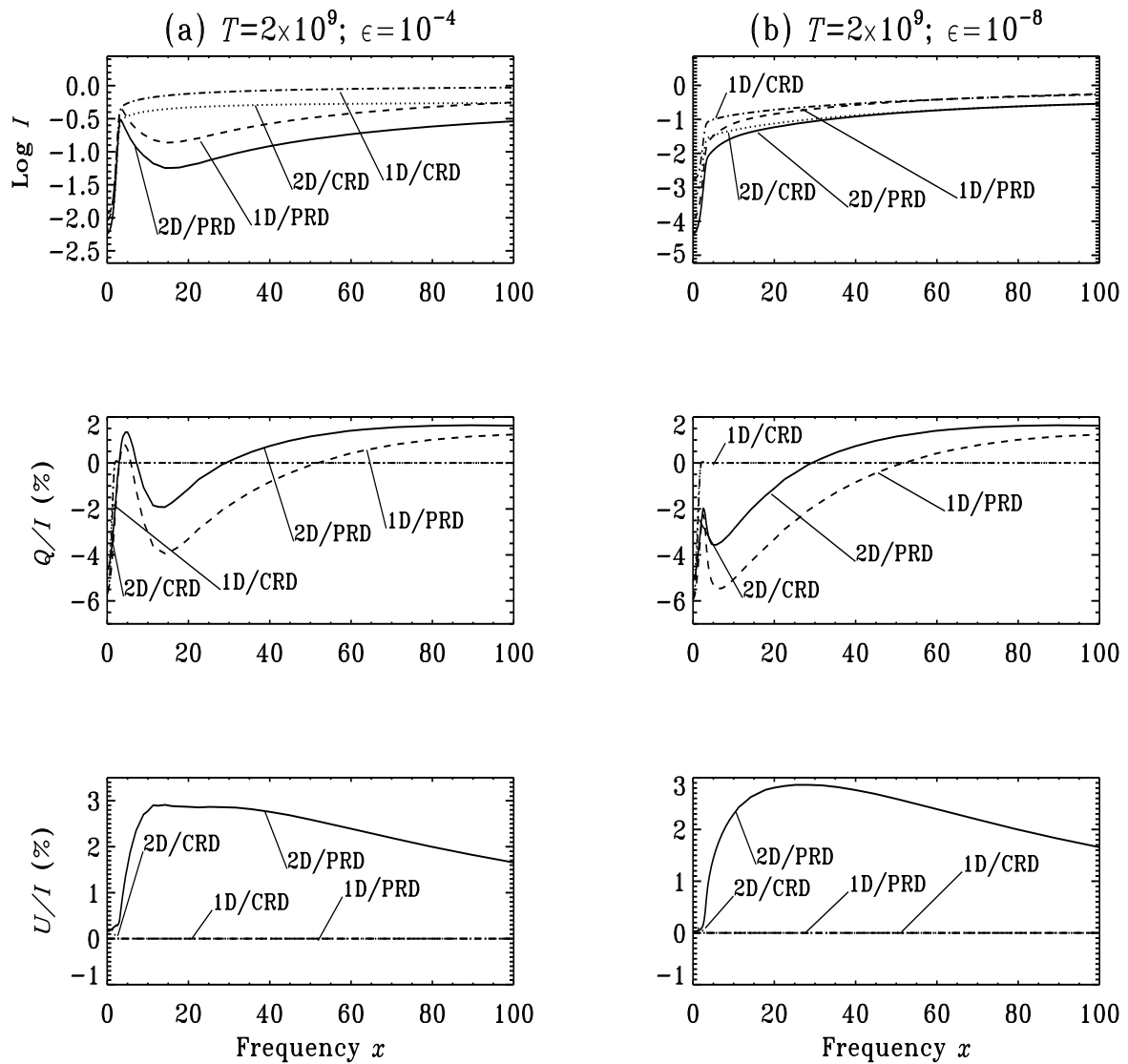


Fig. 9.— The important differences between CRD and PRD Stokes profiles in a semi-infinite 2D atmosphere. The results are shown for  $\mu = 0.11$  and  $\varphi=59.9^\circ$ . The 1D results are shown for comparison. The results are presented for two values of  $\epsilon$ . The model parameters are same as those in Figure 8.